Constitutive Modeling and Algorithmic Implementation of a Plasticity-Like Model for Trabecular Bone Structures

ATUL GUPTA

Orthopaedic Biomechanics Laboratory, University of California, Berkeley, CA, USA 94720.

atulg@berkeley.edu
Ph: 510-642-3787
Fax: 510-642-6163

HARUN H. BAYRAKTAR

ABAQUS, Inc., Providence, RI, USA 02909.

Orthopaedic Biomechanics Laboratory, University of California, Berkeley, CA, USA 94720.

Computational Solid Mechanics Laboratory, University of California, Berkeley, CA, USA 94720.

harun.bayraktar@abaqus.com

JULIA C. FOX

Piziali & Associates, San Carlos, CA, USA 94070.

Orthopaedic Biomechanics Laboratory, University of California, Berkeley, CA, USA 94720.

FoxJ@piziali.com

TONY M. KEAVENY

Department of Mechanical Engineering, University of California, Berkeley, CA, USA 94720.

Department of Bioengineering, University of California, Berkeley, CA, USA 94720.

Orthopaedic Biomechanics Laboratory, University of California, Berkeley, CA, USA 94720.

tmk@me.berkeley.edu
Ph: 510-643-8017
Fax: 510-642-6163

PANAYIOTIS PAPADOPOULOS (Corresponding Author)

Department of Mechanical Engineering, University of California, Berkeley, CA, USA 94720.

Computational Solid Mechanics Laboratory, University of California, Berkeley, CA, USA 94720.

panos@me.berkeley.edu
Ph: 510-642-3358
Fax: 510-642-6163

Abstract

Trabecular bone is a highly porous orthotropic cellular solid material present inside human bones such as the femur (hip bone) and vertebra (spine). In this study, an infinitesimal plasticity-like model with isotropic/kinematic hardening is developed to describe yielding of trabecular bone at the continuum level. One of the unique features of this formulation is the development of the plasticity-like model in strain space for a yield envelope expressed in terms of principal strains having asymmetric yield behavior. An implicit return-mapping approach is adopted to obtain a symmetric algorithmic tangent modulus and a step-by-step procedure of algorithmic implementation is derived. To investigate the performance of this approach in a full-scale finite element simulation, the model is implemented in a non-linear finite element analysis program and several test problems including the simulation of loading of human femur structures are analyzed. The results show good agreement with experimental data.

Keywords

Strain-space plasticity

Finite element analysis

Multiaxial yield envelope

Proximal femur

Bone mechanics

1 Introduction

Osteoporotic hip fractures are the most common serious injury for the elderly [1, 2], associated with substantial socioeconomic consequences. According to the American Academy of Orthopaedic Surgeons, over 350,000 hip fractures occur every year with an estimated cost of over $10 billion; almost one in four hip fracture patients die within one year, and this problem is expected to worsen as the size of the elderly population increases. The finite element technique has been widely used to elucidate the mechanisms of these fractures through the study of the mechanical behavior of the proximal femur under non-habitual (i.e., traumatic) loading conditions, such as those caused by sideways falls [3-5].

Trabecular bone (Fig. 1), a highly porous biological tissue with open-celled cellular structure, is a major load-carrying component in the femur as well as in other whole bones. It is essentially an orthotropic material which exhibits tension-compression asymmetry in yield strength [6]. It has been experimentally established that the yield stress of trabecular bone is highly heterogeneous within and across different anatomic sites, while the yield strain is uniform within any given anatomic site [7, 8]. To properly predict the failure behavior of the femur and other whole bones using continuum finite element models, it is necessary to accurately capture the nonlinear mechanical behavior of trabecular bone at the continuum level [5, 9-12]. Such modeling may also be helpful in orthopaedic implant design, because implant loosening is associated with multiaxial interface stresses on the trabecular bone [13].

In the biomechanics literature, it is common to use a plasticity-like yield function to model the envelope of bone failure, although it is clear that the relevant inelastic process is different from that of classical metal plasticity. While a number of approaches have been adopted for the constitutive modeling of trabecular bone within whole bone finite element models [3, 5, 14], to date no multiaxial constitutive model has been implemented that captures the anisotropy, asymmetry, and heterogeneity of trabecular strength. Several studies conducted on failure load prediction of the femur using nonlinear models have

employed stress-based failure theories assuming isotropic behavior for trabecular bone [3, 5, 14], whereas trabecular bone is an orthotropic material [15-17]. Although trabecular bone is stronger in compression than in tension [18, 19], some of these studies have used the von Mises failure criterion that assumes equal compressive and tensile strength [14, 20]. Further, it has been demonstrated that the use of the von Mises criterion for trabecular bone yielding results in overestimation of stresses when high shear stresses are present [10, 21]. Recently, a multiaxial yield criterion (Fig. 2) has been developed for the femoral neck trabecular bone [22]. This “Modified Super-Ellipsoid” (MSE) criterion is formulated in terms of principal strains because it is found experimentally that the strain-space formulation eliminates the heterogeneity effect from the failure behavior of trabecular bone within an anatomic site [7, 8], thus can be applied to specimens of different porosity. The criterion also exploits the fact that yield strains are uniform in all three principal material directions. While this yield envelope can be used in a plasticity-like formulation of trabecular bone at the continuum level, limited work has been done in the area of strain-based plasticity-like formulations for a yield envelope expressed in the principal space. Furthermore, trabecular bone is known to fail in an uncoupled fashion under multiaxial loads, i.e., despite yielding in one direction, near intact properties are preserved in other directions [22, 23].

The overall goal of this study is to develop a rate-independent infinitesimal plasticity-like model for yielding of trabecular bone in strain space incorporating anisotropy and the MSE multiaxial yield criterion. Specifically, the objectives are to: 1) formulate a rate-independent plasticity-like model in strain space using the MSE multiaxial yield envelope with general parameters and including both kinematic and isotropic hardening; 2) implement an integration algorithm using an implicit return mapping scheme in a finite element analysis program; and 3) use the plasticity-like material model for whole bone analyses of the proximal femur and evaluate its performance with respect to experimental results. The proposed constitutive model is novel in its formulation of infinitesimal strain-based plasticity for a yield envelope expressed in terms of principal strains that departs from the conventional von Mises model (J2-plasticity).

2 Theory

Trabecular bone (Fig. 1) is a heterogeneous material that has a plate and rod-like cellular solid-type structure with a tensile strength lower than its compressive strength. In a previous study [22], a yield envelope (Fig. 2) was obtained in strain space for 5 mm cube specimens of human femoral trabecular bone using high-resolution finite element analyses as a surrogate for experiments. Further, a super-ellipsoid equation [24] was modified and fit to this yield envelope to mathematically express it in terms of certain experimentally measured parameters in the following form [22]

$$g(\varepsilon_1,\varepsilon_2,\varepsilon_3)=\sum_{i=1}^{3}\left|\frac{\varepsilon_i-c}{r}\right|^{2/n}+\left|t\frac{\mathrm{tr}(\boldsymbol{\varepsilon})}{3r}\right|^{2/n}-1. \tag{1}$$

Here, ε_i (i=1, 2, 3) are the principal values of the complete strain tensor $\boldsymbol{\varepsilon}$, r is the radius of the super-ellipsoid, c is the shift in the center coordinates with respect to the origin, n is a “squareness” parameter, and t is a “flattening” parameter. In this model, the radius and shift in center directly correspond to the yield strains and their asymmetry in tension and compression (Fig. 2). This yield envelope captures the micromechanics of trabecular bone at the tissue-level and departs from the Mises-like ellipsoidal form. Further, it exhibits squareness at the corner of tension-shear quadrant (Fig. 2). It is observed from this envelope that the yield behavior of trabecular bone is isotropic when expressed in terms of principal strains with tension-compression yield asymmetry. This observation is supported by various experimental and computational studies [6, 22, 25, 26], which included the detailed tissue-level properties and trabeculae architecture to capture the exact mechanical behavior of trabecular bone at the microstructural level.

In this work, the infinitesimal plasticity-like model in strain space is first developed for a generalized yield envelope. Subsequently, a specific form of this model is derived for the yield envelope formulated in principal strain space based on equation (1), which may be used for whole bone analyses at the continuum level (Fig. 3). It is assumed that the yield envelope specified in equation (1) contains all the microstructural information of trabecular bone and the continuum-level model developed here would be employed for the purpose of nonlinear analyses at the whole-bone-level. Since this is the first step

toward the development of a complete constitutive model for the trabecular bone, damage in bone and effects of bone remodeling at the tissue-level are not included. In addition, post-yield behavior is modeled using hardening. While the latter does not capture the stress reduction that can occur in trabecular bone after the ultimate yield point, it is a commonly used strategy in whole bone mechanics and is considered acceptable at this phase of the constitutive model development. Further, this study is motivated towards capturing the yield behavior and not the post-ultimate fracture behavior of trabecular bone.

In what follows, the notation that all the boldface lower-case letters represent second-order tensors and boldface upper-case letters represent fourth-order tensors is used.

It is observed in the experiments that the trabecular bone behaves nonlinearly under tensile/compressive loading [27] exhibiting minor increase in load carrying capacity after yield and then reduction in stress beyond the ultimate point. After the slight stress reduction trabecular bone continue to sustain appreciable load due to their cellular solid nature. To capture the negligible increase in load carrying capacity and for the reasons of completeness, hardening has been included in this model. Softening behavior has not been included at this juncture due to lack of detailed post-failure three-dimensional stress response of trabecular bone. Therefore, accounting for hardening effects a generalized yield surface in strain space can be written as

$$g = g(\boldsymbol{\varepsilon}^e, \boldsymbol{\alpha}, \beta), \tag{2}$$

where $\boldsymbol{\varepsilon}^e$ is the elastic strain tensor, and $\boldsymbol{\alpha}$ and β are strain-like kinematic and isotropic hardening variables, respectively. The constitutive equation for stress ($\boldsymbol{\sigma}$) assuming additive decomposition of strains into elastic and plastic (inelastic) parts, can be written using the Hooke's law as

$$\boldsymbol{\sigma} = \mathbf{C}^e : (\boldsymbol{\varepsilon} - \boldsymbol{\varepsilon}^p) = \mathbf{C}^e : \boldsymbol{\varepsilon}^e, \tag{3}$$

where $\mathbf{C}^e$ is the fourth-order elasticity tensor and $\boldsymbol{\varepsilon}^e$, $\boldsymbol{\varepsilon}^p$ are the elastic and plastic strain tensors, respectively. Due to lack of any experimental evidence, the flow rule is assumed

to be associative owing to its inherent mathematical simplicity and ease of implementation. Its general form in stress and strain space is written as

$$\dot{\boldsymbol{\varepsilon}}^{p} = \mu \frac{\partial f}{\partial \boldsymbol{\sigma}} = \mu \mathbf{D}^{e} : \frac{\partial g}{\partial \boldsymbol{\varepsilon}^{e}}, \tag{4}$$

where $\mathbf{D}^{e} = (\mathbf{C}^{e})^{-1}$, f is the yield surface in stress space, and μ is the plastic consistency parameter.

Similarly, the hardening rules can be written in the following form

$$\begin{aligned} \dot{\boldsymbol{\alpha}} &= \mu H_{kin} \mathbf{D}^{e} : \frac{\partial g}{\partial \boldsymbol{\alpha}}, \\ \dot{\beta} &= \mu H_{iso} D^{e}_{norm} \frac{\partial g}{\partial \beta}. \end{aligned} \tag{5}$$

Here, H_{kin} and H_{iso} are the kinematic and isotropic hardening parameters, respectively, and D^{e}_{norm} is a scalar multiplication factor introduced to maintain consistency with the units of μ. The associativity of the hardening rules ensures symmetry of the algorithmic tangent moduli [28].

3 Return-mapping algorithm

The return-mapping algorithm is widely used to numerically integrate the differential equations in rate independent plasticity. This approach is well-established and, under certain conditions, ensures a stable and accurate integration of the constitutive equation [28]. An implicit return-mapping approach is adopted which preserves the symmetry of algorithmic tangent moduli (Appendix A). In the return-mapping algorithm, the state variable values ($\boldsymbol{\varepsilon}^{e}, \boldsymbol{\alpha}, \beta$) from the previous converged step are used in determining those values for the current iteration. A step-by-step procedure is derived as shown below for the proposed plasticity-like model.

The yield envelope for the step n+1 can be written as

$$g_{n+1} = g(\boldsymbol{\varepsilon}^e_{n+1}, \boldsymbol{\alpha}_{n+1}, \beta_{n+1}). \tag{6}$$

Equations (4) and (5) can be cast in residual form as

$$\begin{aligned}
\mathbf{R}_{n+1} &= -\boldsymbol{\varepsilon}^p_{n+1} + \boldsymbol{\varepsilon}^p_n + \Delta\mu_{n+1}\mathbf{D}^e : \partial_{\boldsymbol{\varepsilon}^e} g(\boldsymbol{\varepsilon}^e_{n+1}, \boldsymbol{\alpha}_{n+1}, \beta_{n+1}) = \mathbf{0}, \\
\mathbf{S}_{n+1} &= -\boldsymbol{\alpha}_{n+1} + \boldsymbol{\alpha}_n + \Delta\mu_{n+1}H_{kin}\mathbf{D}^e : \partial_{\boldsymbol{\alpha}} g(\boldsymbol{\varepsilon}^e_{n+1}, \boldsymbol{\alpha}_{n+1}, \beta_{n+1}) = \mathbf{0}, \\
T_{n+1} &= -\beta_{n+1} + \beta_n + \Delta\mu_{n+1}H_{iso}D^e_{norm}\partial_\beta g(\boldsymbol{\varepsilon}^e_{n+1}, \boldsymbol{\alpha}_{n+1}, \beta_{n+1}) = 0,
\end{aligned} \tag{7}$$

where $\mathbf{R}_{n+1}$, $\mathbf{S}_{n+1}$ and T_{n+1} are residuals of plastic strain, kinematic hardening and isotropic hardening variables, respectively, at the step n+1. Also, during the plastic corrector phase the total strain is fixed therefore,

$$\Delta\boldsymbol{\varepsilon}^e_{n+1} = -\Delta\boldsymbol{\varepsilon}^p_{n+1}. \tag{8}$$

Upon linearizing and combining equations (6) to (8) for k^{th} iteration, it is readily found that

$$\begin{aligned}
&\mathbf{R}^{(k)} - \Delta\boldsymbol{\varepsilon}^{p^{(k)}} + \Delta\mu^{(k)}\mathbf{D}^e : (-\partial_{\boldsymbol{\varepsilon}^e\boldsymbol{\varepsilon}^e} g^{(k)} : \Delta\boldsymbol{\varepsilon}^{p^{(k)}} + \partial_{\boldsymbol{\varepsilon}^e\boldsymbol{\alpha}} g^{(k)} : \Delta\boldsymbol{\alpha}^{(k)} + \partial_{\boldsymbol{\varepsilon}^e\beta} g^{(k)}\Delta\beta^{(k)}) + \delta\mu^{(k)}\mathbf{D}^e : \partial_{\boldsymbol{\varepsilon}^e} g^{(k)} = \mathbf{0}, \\
&\mathbf{S}^{(k)} - \Delta\boldsymbol{\alpha}^{(k)} + \Delta\mu^{(k)}H_{kin}\mathbf{D}^e : (-\partial_{\boldsymbol{\alpha}\boldsymbol{\varepsilon}^e} g^{(k)} : \Delta\boldsymbol{\varepsilon}^{p^{(k)}} + \partial_{\boldsymbol{\alpha}\boldsymbol{\alpha}} g^{(k)} : \Delta\boldsymbol{\alpha}^{(k)} + \partial_{\boldsymbol{\alpha}\beta} g^{(k)}\Delta\beta^{(k)}) + \delta\mu^{(k)}H_{kin}\mathbf{D}^e : \partial_{\boldsymbol{\alpha}} g^{(k)} = \mathbf{0}, \\
&T^{(k)} - \Delta\beta^{(k)} + \Delta\mu^{(k)}H_{iso}D^e_{norm}(-\partial_{\beta\boldsymbol{\varepsilon}^e} g^{(k)} : \Delta\boldsymbol{\varepsilon}^{p^{(k)}} + \partial_{\beta\boldsymbol{\alpha}} g^{(k)} : \Delta\boldsymbol{\alpha}^{(k)} + \partial_{\beta\beta} g^{(k)}\Delta\beta^{(k)}) + \delta\mu^{(k)}H_{iso}D^e_{norm}\partial_\beta g^{(k)} = 0, \\
&g^{(k)} - \partial_{\boldsymbol{\varepsilon}^e} g^{(k)} : \Delta\boldsymbol{\varepsilon}^{p^{(k)}} + \partial_{\boldsymbol{\alpha}} g^{(k)} : \Delta\boldsymbol{\alpha}^{(k)} + \partial_\beta g^{(k)}\Delta\beta^{(k)} = 0,
\end{aligned} \tag{9}$$

where, for notational simplicity, the subscripts n+1 are dropped. Solving for the unknowns, $\delta\mu^{(k)}, \Delta\boldsymbol{\varepsilon}^{p^{(k)}}$, $\Delta\boldsymbol{\alpha}^{(k)}$ and $\Delta\beta^{(k)}$ leads to

$$\begin{aligned}
\delta\mu^{(k)} &= \frac{-g^{(k)} - \{\partial\mathbf{g}\}^{(k)}\,\mathbf{A}^{(k)}\,\{\tilde{\mathbf{a}}\}^{(k)}}{\{\partial\mathbf{g}\}^{(k)}\,\mathbf{A}^{(k)}\,\{\tilde{\mathbf{r}}\}^{(k)}}, \\
\begin{pmatrix} \Delta\boldsymbol{\varepsilon}^{p^{(k)}} \\ \Delta\boldsymbol{\alpha}^{(k)} \\ \Delta\beta^{(k)} \end{pmatrix} &= \mathbf{A}^{(k)}\{\tilde{\mathbf{a}}\}^{(k)} + \delta\mu^{(k)}\mathbf{A}^{(k)}\{\tilde{\mathbf{r}}\}^{(k)},
\end{aligned} \tag{10}$$

where

$$\left[\mathbf{A}^{(k)}\right]^{-1}=\begin{bmatrix} \mathbf{I}+\Delta\mu^{(k)}\mathbf{D}^e\partial_{\boldsymbol{\varepsilon}^e\boldsymbol{\varepsilon}^e}g^{(k)} & -\Delta\mu^{(k)}\mathbf{D}^e\partial_{\boldsymbol{\varepsilon}^e\boldsymbol{\alpha}}g^{(k)} & -\Delta\mu^{(k)}\mathbf{D}^e\partial_{\boldsymbol{\varepsilon}^e\beta}g^{(k)} \\ \Delta\mu^{(k)}H_{kin}\mathbf{D}^e\partial_{\boldsymbol{\alpha}\boldsymbol{\varepsilon}^e}g^{(k)} & \mathbf{I}-\Delta\mu^{(k)}H_{kin}\mathbf{D}^e\partial_{\boldsymbol{\alpha}\boldsymbol{\alpha}}g^{(k)} & -\Delta\mu^{(k)}H_{kin}\mathbf{D}^e\partial_{\boldsymbol{\alpha}\beta}g^{(k)} \\ \Delta\mu^{(k)}H_{iso}D^e_{norm}\partial_{\beta\boldsymbol{\varepsilon}^e}g^{(k)} & -\Delta\mu^{(k)}H_{iso}D^e_{norm}\partial_{\beta\boldsymbol{\alpha}}g^{(k)} & 1-\Delta\mu^{(k)}H_{iso}D^e_{norm}\partial_{\beta\beta}g^{(k)} \end{bmatrix}$$

and

$$\left\{\tilde{\mathbf{a}}\right\}^{(k)}=\begin{pmatrix}\mathbf{R}^{(k)}\\ \mathbf{S}^{(k)}\\ T^{(k)}\end{pmatrix},\ \left\{\tilde{\mathbf{r}}\right\}^{(k)}=\begin{pmatrix}\mathbf{D}^e:\partial_{\boldsymbol{\varepsilon}^e}g^{(k)}\\ H_{kin}\mathbf{D}^e:\partial_{\boldsymbol{\alpha}}g^{(k)}\\ H_{iso}D^e_{norm}\partial_{\beta}g^{(k)}\end{pmatrix},\ \left\{\partial\mathbf{g}\right\}^{(k)}=\begin{bmatrix}-\partial_{\boldsymbol{\varepsilon}^e}g^{(k)} & \partial_{\boldsymbol{\alpha}}g^{(k)} & \partial_{\beta}g^{(k)}\end{bmatrix}.$$

Using these expressions the state variables in incremental form are updated as

$$\begin{aligned}
&\boldsymbol{\varepsilon}^{p^{(k+1)}}=\boldsymbol{\varepsilon}^{p^{(k)}}+\Delta\boldsymbol{\varepsilon}^{p^{(k)}},\\
&\boldsymbol{\alpha}^{(k+1)}=\boldsymbol{\alpha}^{(k)}+\Delta\boldsymbol{\alpha}^{(k)},\\
&\beta^{(k+1)}=\beta^{(k)}+\Delta\beta^{(k)},\\
&\Delta\mu^{(k+1)}=\Delta\mu^{(k)}+\delta\mu^{(k)}.
\end{aligned}\tag{11}$$

The detailed steps of the return-mapping algorithm are presented in Box 1.

4 Application to trabecular bone modeling

The yield equation (1) including hardening parameters can be rewritten as

$$g=\sum_{i=1}^{3}\sqrt[n]{\left(\gamma_i-c\right)^2}+\sqrt[n]{\left(t\frac{\mathrm{tr}(\boldsymbol{\gamma})}{3}\right)^2}-\sqrt[n]{\left(r+\beta\right)^2},\tag{12}$$

where $\boldsymbol{\gamma}=\boldsymbol{\varepsilon}^e-\boldsymbol{\alpha}$ and γ_i are the principal values of $\boldsymbol{\gamma}$. Using the above relations and the chain rule leads to

$$\begin{aligned}
&\partial_{\boldsymbol{\varepsilon}^e\boldsymbol{\varepsilon}^e}g=\partial_{\gamma\gamma}g,\\
&\partial_{\boldsymbol{\varepsilon}^e\boldsymbol{\alpha}}g=\partial_{\boldsymbol{\alpha}\boldsymbol{\varepsilon}^e}g=-\partial_{\gamma\gamma}g,\\
&\partial_{\boldsymbol{\varepsilon}^e\beta}g=\partial_{\beta\boldsymbol{\varepsilon}^e}g=\mathbf{0},\\
&\partial_{\boldsymbol{\alpha}\boldsymbol{\alpha}}g=\partial_{\gamma\gamma}g,\\
&\partial_{\boldsymbol{\alpha}\beta}g=\partial_{\beta\boldsymbol{\alpha}}g=\mathbf{0}.
\end{aligned}\tag{13}$$

Taking into account equations (10) and (13), $\mathbf{A}^{-1}$ may be rewritten as

$$\mathbf{A}^{-1}=\begin{bmatrix}\mathbf{I}+\Delta\mu\mathbf{D}^e\partial_{\gamma\gamma}g & \Delta\mu\mathbf{D}^e\partial_{\gamma\gamma}g & \mathbf{0}\\ -\Delta\mu H_{kin}\mathbf{D}^e\partial_{\gamma\gamma}g & \mathbf{I}-\Delta\mu H_{kin}\mathbf{D}^e\partial_{\gamma\gamma}g & \mathbf{0}\\ \mathbf{0} & \mathbf{0} & 1-\Delta\mu H_{iso}D^e_{norm}\partial_{\beta\beta}g\end{bmatrix}, \tag{14}$$

where the superscript (k) is omitted for brevity. Therefore, $\mathbf{A}$ can be deduced from the above equation as

$$\mathbf{A}=\begin{bmatrix}\mathbf{A}_2\mathbf{A}_1 & -\mathbf{A}_3\mathbf{A}_1 & \mathbf{0}\\ \mathbf{A}_4\mathbf{A}_1 & \mathbf{A}_5\mathbf{A}_1 & \mathbf{0}\\ \mathbf{0} & \mathbf{0} & A_6\end{bmatrix}, \tag{15}$$

where

$$\mathbf{A}_1=\left[\mathbf{D}^e+\Delta\mu(1-H_{kin})\mathbf{D}^e\partial_{\gamma\gamma}g\mathbf{D}^e\right]^{-1},$$
$$\mathbf{A}_2=\mathbf{D}^e-\Delta\mu H_{kin}\mathbf{D}^e\partial_{\gamma\gamma}g\mathbf{D}^e,$$
$$\mathbf{A}_3=\Delta\mu\mathbf{D}^e\partial_{\gamma\gamma}g\mathbf{D}^e,$$
$$\mathbf{A}_4=\Delta\mu H_{kin}\mathbf{D}^e\partial_{\gamma\gamma}g\mathbf{D}^e,$$
$$\mathbf{A}_5=\mathbf{D}^e+\Delta\mu\mathbf{D}^e\partial_{\gamma\gamma}g\mathbf{D}^e,$$
$$A_6=(1-\Delta\mu H_{iso}D^e_{norm}\partial_{\beta\beta}g)^{-1}.$$

The algorithmic tangent modulus for this model is derived in Appendix A.

This derivation also involves the calculation of the first and second derivatives of the yield function g with respect to the strain-like tensor $\boldsymbol{\gamma}$, where g is an isotropic function of the principal values of $\boldsymbol{\gamma}$. The first derivative can be written as

$$\frac{\partial g}{\partial\boldsymbol{\gamma}}=\sum_{A=1}^{3}\frac{\partial g}{\partial\gamma_A}\mathbf{m}^{(A)}, \tag{16}$$

see [29], where γ_A are the principal values and $\mathbf{m}^{(A)}$ are the eigenbases of the tensor $\boldsymbol{\gamma}$. The second derivatives are computed for distinct and non-zero principal values of $\boldsymbol{\gamma}$ as

$$\frac{\partial^2 g}{\partial\boldsymbol{\gamma}^2}=\sum_{A=1}^{3}\sum_{B=1}^{3}\frac{\partial_{\gamma_A}g}{\partial\gamma_B}\mathbf{m}^{(A)}\otimes\mathbf{m}^{(B)}+\sum_{A=1}^{3}\frac{\partial g}{\partial\gamma_A}\frac{\partial\mathbf{m}^{(A)}}{\partial\boldsymbol{\gamma}}, \tag{17}$$

see [29-31], where an explicit expression for $\frac{\partial \mathbf{m}^{(A)}}{\partial \boldsymbol{\gamma}}$ is obtained as

$$\begin{aligned}\frac{\partial \mathbf{m}^{(A)}}{\partial \boldsymbol{\gamma}} = \Big[& \mathbf{I}_e - (I_1 - \gamma_A)\mathbf{I} - \boldsymbol{\gamma} \otimes \mathbf{1} + \boldsymbol{\gamma} \otimes \mathbf{m}^{(A)} + I_3 \gamma_A^{-1} \mathbf{1} \otimes \boldsymbol{\gamma}^{-1} - I_3 \gamma_A^{-2} \mathbf{1} \otimes \mathbf{m}^{(A)} \\ & + \gamma_A \mathbf{m}^{(A)} \otimes \mathbf{1} - I_3 \gamma_A^{-1} \mathbf{m}^{(A)} \otimes \boldsymbol{\gamma}^{-1} + \psi \mathbf{m}^{(A)} \otimes \mathbf{m}^{(A)} \Big] / D_A,\end{aligned} \tag{18}$$

in terms of the three invariants I_1, I_2, I_3 of $\boldsymbol{\gamma}$, the second-order identity $\mathbf{1}$ and the fourth-order identity $\mathbf{I}$. In addition, equation (18) makes use of the following quantities

$$D_A = 2\gamma_A^2 - I_1 \gamma_A + I_3 \gamma_A^{-1} \neq 0,$$
$$\mathbb{I}_{(e)ijkl} = \frac{1}{2}\left(\delta_{ik}\gamma_{jl} + \delta_{il}\gamma_{jk}\right) + \frac{1}{2}\left(\gamma_{ik}\delta_{jl} + \gamma_{il}\delta_{jk}\right),$$
$$\psi = I_1 + I_3 \gamma_A^{-2} - 4\gamma_A.$$

This equation becomes indeterminate for equal or zero principal values and special forms of it for these cases are discussed in Appendix B.

5 Algorithmic Implementation

The plasticity-like model derived in the previous section is implemented in FEAP, a fully nonlinear finite element code documented in [32]. To include material anisotropy, the fourth-order elasticity tensor $\mathbf{C}^e$ in the principal material coordinate system is rotated to the global mesh coordinate system using known material orientations and then used in the plasticity algorithm to update state variables for each integration point. Representative simulations are conducted to test the accuracy and behavior of the model and to ensure numerical convergence and applicability to the finite element modeling of human proximal femur. Eight-node hexahedral elements are used for all simulations. The Newton-Raphson scheme is employed to solve the nonlinear system emanating from the weak form of the equilibrium equations.

5.1 Homogeneous strain cycle

This problem consists of a single brick element subjected to cyclic pure tension-compression displacement boundary conditions. Generic elastic material properties are

assigned to this element, in which the material is assumed to be isotropic with Young's modulus E=1000 MPa and Poisson's ratio ν=0.3. The parameters *r*, *c*, *n* and *t* of yield envelope (Table 1) are assumed to be the same as for the trabecular bone previously determined by Bayraktar *et al.* [22]. Four test cases are considered assuming: 1) the elastic perfectly plastic material behavior; 2) the kinematic hardening 0.1 times the elastic modulus (H_{kin}=0.1); 3) the isotropic hardening 0.1 times the elastic modulus (H_{iso}=0.1); and 4) both kinematic and isotropic hardening (H_{kin}=0.05, H_{iso}=0.05). The material behavior (stresses and strains) at one of the integration points is shown in Fig. 4.

This plasticity-like model under cyclic loading captures the expected behavior with the kinematic and isotropic hardening, as well as the tension-compression yield strength asymmetry (Fig. 4). The yield envelope is stationary in the elastic perfectly plastic case. A shift is observed in the yield envelope in the pure kinematic hardening case. The size of the yield envelope increases under pure isotropic hardening. The yield values are also in agreement with the analytical predictions.

5.2 Solid cube under triaxial strain

In this problem, a 4 x 4 x 4 mm solid cube with 1 x 1 x 1 mm brick elements is subjected to uniform triaxial compression displacement boundary condition. Orthotropic material properties: E_1=2376 MPa, E_2=1377 MPa, E_3=3645 MPa, ν_{12}=0.28, ν_{23}=0.14, ν_{13}=0.15, G_{12}=616 MPa, G_{23}=784 MPa, and G_{13}=1193 MPa, similar to trabecular bone are assigned to each element and the parameters *r*, *c*, *n* and *t* are taken from Table 1. This problem is solved in FEAP with H_{kin}=0.05 and H_{iso}=0.05.

The stress-strain curves obtained in the three directions are shown in Fig. 5. In all three directions, the model failed at the same strain because of the isotropy of the yield envelope in strain space but at different stresses due to material orthotropy (Fig. 5). This result is in agreement with the behavior of the plasticity-like model presented here.

5.3 Nonlinear analysis of a human proximal femur

A proximal femur obtained from an 86-year-old female human cadaver is scanned with Quantitative Computed Tomography (QCT, Somatom Plus 4, Siemens Medical, Erlangen, Germany) at 120 kVp, 240 mA, (0.2 mm in-plane and 1 mm out-of-plane voxel size), and again with micro-Computed Tomography (micro-CT) using a cubic voxel size of approximately 90 microns (Radios, SCANCO Medical AG, Bassersdorf, Switzerland) (Fig. 1). Three-dimensional voxel-based finite element models (Fig. 6) are generated from QCT scans by coarsening these images, i.e., collapsing the image voxels in all directions, and converting these coarsened voxels directly into 8-noded brick elements with element size ranging from 1.9335 x 1.9335 x 2.0 to 5.0271 x 5.0271 x 5.0 mm having 1,028 to 17,516 elements.

The bone apparent density, ρ (in g/cm^3) of each element is determined from the QCT scans using a regression between the known apparent density values and the corresponding pixel intensities in Hounsfield Units (HU). The regression is created by linearly correlating mean HU values in the trochanteric and femoral neck regions of the proximal femur to the mean apparent density values for these regions, as calculated in a large cross-sectional study [7]. The primary elastic modulus (E_1, in MPa) is assigned to each element using apparent density-modulus relationship determined from on-axis mechanical tests of trabecular bone cores from the greater trochanter and femoral neck [7, 26] as

$$E_1 = \begin{cases} c_1\rho^{\alpha_1}, & \text{for } \rho \le 0.32 \text{ g/cm}^3 \\ c_2\rho^{\alpha_2}, & \text{for } \rho > 0.32 \text{ g/cm}^3 \end{cases}$$

Here α_1 =15010 and α_2 =6850 are dimensionless constants, while c_1 =2.18 and c_1 =1.49 have units of square of velocity. The principal values and directions that characterize the microstructural anisotropic orientation of trabecular bone as well as the volume fraction are determined uniquely for each element in the finite element mesh using the mean intercept length tensor [33] measured from the micro-CT scans in 4 mm cube regions throughout the proximal femur [34]. Element-specific orthotropic elastic constants are

then assigned to each element using published relations between volume fraction and the elastic modulus in the principal material direction [35].

A stance-type displacement boundary condition (Fig. 6) is applied to these models by fixing the distal end and applying a distributed compressive load at an angle of 20^o to nodes on the superior aspect of the femoral head [36]. Muscle forces are avoided to match FE simulations with the simplified boundary conditions used in the experiments. Nonlinear analyses are performed on these models using FEAP with both isotropic and kinematic hardening (H_{kin}=0.005, H_{iso}=0.005).

The yield force values of the femur are calculated from the force-deformation curve using a 90% secant method. This measure displays convergence, as the mesh is refined (Fig. 7). The yield force for the finest mesh is in close agreement with the experimental result. The convergence of the residual norm for this problem is quadratic and the force-deformation curve (Fig. 7) shows that the solution at each step is stable.

6 Conclusions

This article presents a constitutive and computational framework for the analysis of a cellular solid-type material with a yield envelope expressed in terms of principal strains. The material anisotropy in stress space is also incorporated in our model by rotation of the anisotropic fourth-order elasticity tensor from the principal material coordinate system to the global mesh coordinate system. A detailed procedure is derived for this plasticity-like model to facilitate algorithmic implementation. From a computational standpoint, the method developed here preserves the structure of return-mapping algorithm used widely for the stress- and strain-based plasticity formulations. A numerically stable implicit approach results in a robust formulation ensuring quadratic convergence for the Newton-Raphson iterative solution strategy. In future studies, the present formulation can be extended to include geometric nonlinearities that might have an effect on lower density trabecular bone found in many sites, and to other applications involving cellular solid materials with different yield envelope and hardening rules. The model could be further refined to include bone remodeling based on mechanical stimuli

and damage behavior, which might play a significant role in the post-yield and reloading behavior of trabecular bone.

Acknowledgements

This study was supported by grant (AR43784) from the National Institutes of Health.

Appendix A. Algorithmic tangent moduli

In the nonlinear finite element analysis, a consistent tangent operator is used for the algorithmic implementation of the solution procedure using iterative strategies such as the Newton-Raphson method. Assuming iterative solution procedure the algorithmic modulus can be defined for the step n+1 as

$$\mathbf{C}^{(alg)} = \left(\frac{d\boldsymbol{\sigma}}{d\boldsymbol{\varepsilon}} \right)_{n+1}. \tag{A.1}$$

Writing equations (3)-(5) in differential form and substituting $d\boldsymbol{\varepsilon}^e = \mathbf{D}^e : d\boldsymbol{\sigma}$ leads to

$$\begin{aligned}
&d\boldsymbol{\sigma} = \mathbf{C}^e : (d\boldsymbol{\varepsilon} - d\boldsymbol{\varepsilon}^p) \Rightarrow d\boldsymbol{\varepsilon}^p = -\mathbf{D}^e : d\boldsymbol{\sigma} + d\boldsymbol{\varepsilon},\\
&d\boldsymbol{\varepsilon}^p = d(\Delta\mu)\mathbf{D}^e : \partial_{\boldsymbol{\varepsilon}^e} g + \Delta\mu \mathbf{D}^e : (\partial_{\boldsymbol{\varepsilon}^e \boldsymbol{\varepsilon}^e} g : \mathbf{D}^e : d\boldsymbol{\sigma} + \partial_{\boldsymbol{\varepsilon}^e \boldsymbol{\alpha}} g : d\boldsymbol{\alpha} + \partial_{\boldsymbol{\varepsilon}^e \beta} g d\beta),\\
&d\boldsymbol{\alpha} = d(\Delta\mu) H_{kin} \mathbf{D}^e : \partial_{\boldsymbol{\alpha}} g + \Delta\mu H_{kin} \mathbf{D}^e : (\partial_{\boldsymbol{\alpha}\boldsymbol{\varepsilon}^e} g : \mathbf{D}^e : d\boldsymbol{\sigma} + \partial_{\boldsymbol{\alpha}\boldsymbol{\alpha}} g : d\boldsymbol{\alpha} + \partial_{\boldsymbol{\alpha}\beta} g d\beta),\\
&d\beta = d(\Delta\mu) H_{iso} D^e_{norm} \partial_\beta g + \Delta\mu H_{iso} D^e_{norm} (\partial_{\beta\boldsymbol{\varepsilon}^e} g : \mathbf{D}^e : d\boldsymbol{\sigma} + \partial_{\beta\boldsymbol{\alpha}} g : d\boldsymbol{\alpha} + \partial_{\beta\beta} g d\beta).
\end{aligned} \tag{A.2}$$

Also, from equation (2) it follows that

$$dg = \mathbf{D}^e : \partial_{\boldsymbol{\varepsilon}^e} g : d\boldsymbol{\sigma} + \partial_{\boldsymbol{\alpha}} g : d\boldsymbol{\alpha} + \partial_\beta g d\beta = 0, \tag{A.3}$$

or, in matrix form,

$$dg = \underbrace{\begin{bmatrix} \mathbf{D}^e : \partial_{\boldsymbol{\varepsilon}^e} g & \partial_{\boldsymbol{\alpha}} g & \partial_\beta g \end{bmatrix}}_{\{\partial \mathbf{g}\}} \begin{pmatrix} d\boldsymbol{\sigma} \\ d\boldsymbol{\alpha} \\ d\beta \end{pmatrix} = 0. \tag{A.4}$$

Likewise, equation (A.2) can be written in the matrix form as

$$\begin{pmatrix} d\boldsymbol{\varepsilon} \\ \mathbf{0} \\ 0 \end{pmatrix} - d(\Delta\mu) \underbrace{\begin{pmatrix} \mathbf{D}^e : \partial_{\boldsymbol{\varepsilon}^e} g \\ \partial_{\boldsymbol{\alpha}} g \\ \partial_\beta g \end{pmatrix}}_{\{\bar{\mathbf{r}}\}} = \underbrace{\begin{bmatrix} \mathbf{D}^e + \Delta\mu \mathbf{D}^e \partial_{\boldsymbol{\varepsilon}^e \boldsymbol{\varepsilon}^e} g \mathbf{D}^e & \Delta\mu \mathbf{D}^e \partial_{\boldsymbol{\varepsilon}^e \boldsymbol{\alpha}} g & \Delta\mu \mathbf{D}^e \partial_{\boldsymbol{\varepsilon}^e \beta} g \\ \Delta\mu \partial_{\boldsymbol{\alpha}\boldsymbol{\varepsilon}^e} g \mathbf{D}^e & -\dfrac{\mathbf{C}^e}{H_{kin}} + \Delta\mu \partial_{\boldsymbol{\alpha}\boldsymbol{\alpha}} g & \Delta\mu \partial_{\boldsymbol{\alpha}\beta} g \\ \Delta\mu \partial_{\beta\boldsymbol{\varepsilon}^e} g \mathbf{D}^e & \Delta\mu \partial_{\beta\boldsymbol{\alpha}} g & -\dfrac{1}{H_{iso} D^e_{norm}} + \Delta\mu \partial_{\beta\beta} g \end{bmatrix}}_{\mathbf{B}^{-1}} \begin{pmatrix} d\boldsymbol{\sigma} \\ d\boldsymbol{\alpha} \\ d\beta \end{pmatrix}. \tag{A.5}$$

or

$$\begin{pmatrix} d\boldsymbol{\sigma} \\ d\boldsymbol{\alpha} \\ d\beta \end{pmatrix} = \mathbf{B} : \begin{pmatrix} d\boldsymbol{\varepsilon} \\ \mathbf{0} \\ 0 \end{pmatrix} - d(\Delta\mu)\mathbf{B} : \{\tilde{\mathbf{r}}\}. \tag{A.6}$$

Combining equations (A.4) and (A.6) to solve for the unknown $d(\Delta\mu)$ results in

$$d(\Delta\mu) = \frac{\{\partial \mathbf{g}\} : \mathbf{B} : \begin{pmatrix} d\boldsymbol{\varepsilon} \\ \mathbf{0} \\ \mathbf{0} \end{pmatrix}}{\{\partial \mathbf{g}\} : \mathbf{B} : \{\tilde{\mathbf{r}}\}}. \tag{A.7}$$

Substitution of the value of $d(\Delta\mu)$ in equation (A.6) results in

$$\begin{pmatrix} d\boldsymbol{\sigma} \\ d\boldsymbol{\alpha} \\ d\beta \end{pmatrix} = \left[\mathbf{B} - \frac{\left(\mathbf{B} : \{\tilde{\mathbf{r}}\}\right) \otimes \left(\{\partial \mathbf{g}\} : \mathbf{B}\right)}{\{\partial \mathbf{g}\} : \mathbf{B} : \{\tilde{\mathbf{r}}\}} \right] \begin{pmatrix} d\boldsymbol{\varepsilon} \\ \mathbf{0} \\ 0 \end{pmatrix}. \tag{A.8}$$

From the above derivation, the algorithmic modulus (consistent tangent operator) can be written as

$$\mathbf{C}^{(alg)} = \left[\mathbf{B} - \frac{\left(\mathbf{B} : \{\tilde{\mathbf{r}}\}\right) \otimes \left(\{\partial \mathbf{g}\} : \mathbf{B}\right)}{\{\partial \mathbf{g}\} : \mathbf{B} : \{\tilde{\mathbf{r}}\}} \right]_{\text{upper } 6x6 \text{ part}}. \tag{A.9}$$

Using equation (13), $\mathbf{B}^{-1}$ from equation (A.5) can be simplified as

$$\mathbf{B}^{-1} = \begin{bmatrix} \mathbf{D}^e + \Delta\mu \mathbf{D}^e \partial_{\gamma\gamma} g \mathbf{D}^e & -\Delta\mu \mathbf{D}^e \partial_{\gamma\gamma} g & \mathbf{0} \\ -\Delta\mu \partial_{\gamma\gamma} g \mathbf{D}^e & -\dfrac{\mathbf{C}^e}{H_{kin}} + \Delta\mu \partial_{\gamma\gamma} g & \mathbf{0} \\ \mathbf{0} & \mathbf{0} & -\dfrac{1}{H_{iso} D^e_{norm}} + \Delta\mu \partial_{\beta\beta} g \end{bmatrix}. \tag{A.10}$$

After inverting, $\mathbf{B}$ is obtained as

$$\mathbf{B} = \begin{bmatrix} \mathbf{B}_1 - \mathbf{B}_1\mathbf{B}_2 & -\mathbf{B}_1\mathbf{B}_3 & \mathbf{0} \\ -\mathbf{B}_3\mathbf{B}_1 & -\mathbf{D}^e\mathbf{B}_1\mathbf{B}_4 & \mathbf{0} \\ \mathbf{0} & \mathbf{0} & B_5 \end{bmatrix}, \tag{A.11}$$

where

$$\mathbf{B}_1 = \left[\mathbf{D}^e + \Delta\mu(1 - H_{kin})\mathbf{D}^e\partial_{\gamma\gamma}g\mathbf{D}^e \right]^{-1},$$
$$\mathbf{B}_2 = \Delta\mu H_{kin}\mathbf{D}^e\partial_{\gamma\gamma}g,$$
$$\mathbf{B}_3 = \Delta\mu H_{kin}\mathbf{D}^e\partial_{\gamma\gamma}g\mathbf{D}^e,$$
$$\mathbf{B}_4 = H_{kin}\mathbf{D}^e + \Delta\mu H_{kin}\mathbf{D}^e\partial_{\gamma\gamma}g\mathbf{D}^e,$$
$$B_5 = H_{iso}D^e_{norm}(\Delta\mu H_{iso}D^e_{norm}\partial_{\beta\beta}g - 1)^{-1}.$$

Appendix B. Second Derivatives

The second derivative of the yield envelope g with respect to $\boldsymbol{\gamma}$ (equation (17)) becomes indeterminate for the case of equal or zero roots of tensor $\boldsymbol{\gamma}$. To avoid the indeterminacy, particular expressions of these derivatives are deduced. In what follows, γ_A are the principal values, $\mathbf{n}^{(A)}$ are the eigenvectors and $\mathbf{m}^{(A)}$ are the eigenbases of tensor $\boldsymbol{\gamma}$.

1. If $\gamma_1 = \gamma_2 \neq \gamma_3$,

$$\begin{aligned}\frac{\partial^2 g}{\partial \boldsymbol{\gamma}^2} = {} & \frac{\partial_{\gamma_1} g}{\partial \gamma_1}\mathbf{1}\otimes\mathbf{1} + \left(\frac{\partial_{\gamma_1} g}{\partial \gamma_3} - \frac{\partial_{\gamma_1} g}{\partial \gamma_1}\right)\mathbf{1}\otimes\mathbf{m}^{(3)} + \left(\frac{\partial_{\gamma_3} g}{\partial \gamma_1} - \frac{\partial_{\gamma_1} g}{\partial \gamma_1}\right)\mathbf{m}^{(3)}\otimes\mathbf{1} \\ & + \left(\frac{\partial_{\gamma_3} g}{\partial \gamma_3} - \frac{\partial_{\gamma_1} g}{\partial \gamma_3} - \frac{\partial_{\gamma_3} g}{\partial \gamma_1} + \frac{\partial_{\gamma_1} g}{\partial \gamma_1}\right)\mathbf{m}^{(3)}\otimes\mathbf{m}^{(3)} + \left(\frac{\partial g}{\partial \gamma_3} - \frac{\partial g}{\partial \gamma_1}\right)\frac{\partial \mathbf{m}^{(3)}}{\partial \boldsymbol{\gamma}},\end{aligned} \tag{B.1}$$

where $\dfrac{\partial \mathbf{m}^{(3)}}{\partial \boldsymbol{\gamma}}$ can be calculated based on equation (18).

2. If $\gamma_1 = \gamma_2 = \gamma_3$,

$$\frac{\partial^2 g}{\partial \boldsymbol{\gamma}^2} = \frac{\partial_{\gamma_1} g}{\partial \gamma_1}\mathbf{1}\otimes\mathbf{1}. \tag{B.2}$$

3. If $\gamma_1 \neq \gamma_2$ and $\gamma_3 = 0$,

$$\frac{\partial_{\boldsymbol{\gamma}} g}{\partial \boldsymbol{\gamma}} = \sum_{A=1}^{3}\sum_{B=1}^{3}\frac{\partial_{\gamma_A} g}{\partial \gamma_B}\mathbf{m}^{(A)}\otimes\mathbf{m}^{(B)} + \frac{1}{2}\sum_{A=1}^{3}\sum_{B\neq A}\frac{\dfrac{\partial g}{\partial \gamma_B} - \dfrac{\partial g}{\partial \gamma_A}}{\gamma_B - \gamma_A}\left(\mathbf{m}^{(AB)}\otimes\mathbf{m}^{(AB)} + \mathbf{m}^{(AB)}\otimes\mathbf{m}^{(BA)}\right), \tag{B.3}$$

where $\mathbf{m}^{(A)} = \mathbf{n}^{(A)}\otimes\mathbf{n}^{(A)}$, $\mathbf{m}^{(AB)} = \mathbf{n}^{(A)}\otimes\mathbf{n}^{(B)}$, $A \neq B$.

4. If $\gamma_1 = \gamma_2 = 0$ and $\gamma_3 \neq 0$,

$$\begin{aligned}\frac{\partial^2 g}{\partial \boldsymbol{\gamma}^2} = {} & \frac{\partial_{\gamma_1} g}{\partial \gamma_1}\mathbf{1}\otimes\mathbf{1} + \left(\frac{\partial_{\gamma_1} g}{\partial \gamma_3} - \frac{\partial_{\gamma_1} g}{\partial \gamma_1}\right)\mathbf{1}\otimes\mathbf{m}^{(3)} + \left(\frac{\partial_{\gamma_3} g}{\partial \gamma_1} - \frac{\partial_{\gamma_1} g}{\partial \gamma_1}\right)\mathbf{m}^{(3)}\otimes\mathbf{1} \\ & + \left(\frac{\partial_{\gamma_3} g}{\partial \gamma_3} - \frac{\partial_{\gamma_1} g}{\partial \gamma_3} - \frac{\partial_{\gamma_3} g}{\partial \gamma_1} + \frac{\partial_{\gamma_1} g}{\partial \gamma_1}\right)\mathbf{m}^{(3)}\otimes\mathbf{m}^{(3)} + \left(\frac{\partial g}{\partial \gamma_3} - \frac{\partial g}{\partial \gamma_1}\right)\frac{\partial \mathbf{m}^{(3)}}{\partial \boldsymbol{\gamma}},\end{aligned} \tag{B.4}$$

where $\dfrac{\partial \mathbf{m}^{(3)}}{\partial \boldsymbol{\gamma}} = \dfrac{1}{\gamma_3}\left(\mathbf{I} - \mathbf{m}^{(3)} \otimes \mathbf{m}^{(3)}\right)$.

5. If $\gamma_1 = \gamma_2$ and $\gamma_3 = 0$,

$$\begin{aligned}\frac{\partial^2 g}{\partial \boldsymbol{\gamma}^2} = {} & \frac{\partial_{\gamma_3} g}{\partial \gamma_3}\mathbf{1}\otimes\mathbf{1} + \left(\frac{\partial_{\gamma_3} g}{\partial \gamma_1} - \frac{\partial_{\gamma_3} g}{\partial \gamma_3}\right)\mathbf{1}\otimes\left(\mathbf{m}^{(1)} + \mathbf{m}^{(2)}\right) + \left(\frac{\partial_{\gamma_1} g}{\partial \gamma_3} - \frac{\partial_{\gamma_3} g}{\partial \gamma_3}\right)\left(\mathbf{m}^{(1)} + \mathbf{m}^{(2)}\right)\otimes\mathbf{1} \\ & + \left(\frac{\partial_{\gamma_1} g}{\partial \gamma_1} - \frac{\partial_{\gamma_3} g}{\partial \gamma_1} - \frac{\partial_{\gamma_1} g}{\partial \gamma_3} + \frac{\partial_{\gamma_3} g}{\partial \gamma_3}\right)\left(\mathbf{m}^{(1)} + \mathbf{m}^{(2)}\right)\otimes\left(\mathbf{m}^{(1)} + \mathbf{m}^{(2)}\right) + \left(\frac{\partial g}{\partial \gamma_1} - \frac{\partial g}{\partial \gamma_3}\right)\frac{\partial\left(\mathbf{m}^{(1)} + \mathbf{m}^{(2)}\right)}{\partial \boldsymbol{\gamma}},\end{aligned} \tag{B.5}$$

where $\dfrac{\partial\left(\mathbf{m}^{(1)} + \mathbf{m}^{(2)}\right)}{\partial \boldsymbol{\gamma}} = \dfrac{1}{\gamma_1}\left(\mathbf{I} - \left(\mathbf{m}^{(1)} + \mathbf{m}^{(2)}\right)\otimes\left(\mathbf{m}^{(1)} + \mathbf{m}^{(2)}\right)\right)$.

References

1. Riggs BL, Melton LJ (1995) The worldwide problem of osteoporosis: insights afforded by epidemiology. Bone 17: 505S-511S.
2. Melton LJ (2003) Adverse outcomes of osteoporotic fractures in the general population. Journal of Bone and Mineral Research 18: 1139-1141.
3. Lotz JC, Cheal EJ, Hayes WC (1991) Fracture prediction for the proximal femur using finite element models: Part II--Nonlinear analysis. Journal of Biomechanical Engineering 113: 361-365.
4. Ford CM, Keaveny TM, Hayes WC (1996) The effect of impact direction on the structural capacity of the proximal femur during falls. Journal of Bone and Mineral Research 11: 377-383.
5. Keyak JH, Rossi SA (2000) Prediction of femoral fracture load using finite element models: an examination of stress- and strain-based failure theories. Journal of Biomechanics 33: 209-214.
6. Keaveny TM (2001) Strength of trabecular bone. In: Cowin SC (editor) Bone mechanics handbook. CRC press, Boca Raton, FL, pp 16-1-42.
7. Morgan EF, Keaveny TM (2001) Dependence of yield strain of human trabecular bone on anatomic site. Journal of Biomechanics 34: 569-577.
8. Bayraktar HH, Keaveny TM (2004) Mechanisms of uniformity of yield strains for trabecular bone. Journal of Biomechanics 37: 1671-1678.
9. Lotz JC, Gerhart TN, Hayes WC (1990) Mechanical properties of trabecular bone from the proximal femur: a quantitative CT study. Journal of Computer Assisted Tomography 14: 107-114.
10. Ford CM, Keaveny TM (1996) The dependence of shear failure properties of bovine tibial trabecular bone on apparent density and trabecular orientation. Journal of Biomechanics 29: 1309-1317.
11. Cody DD, Gross GJ, Hou FJ, Spencer HJ, Goldstein SA, Fyhrie DP (1999) Femoral strength is better predicted by finite element models than QCT and DXA. Journal of Biomechanics 32: 1013-1020.
12. Ciarelli TE, Fyhrie DP, Schaffler MB, Goldstein SA (2000) Variations in three-dimensional cancellous bone architecture of the proximal femur in female hip fractures and in controls. Journal of Bone and Mineral Research 15: 32-40.
13. Cheal EJ, Hayes WC, Lee CH, Snyder BD, Miller J (1985) Stress analysis of a condylar knee tibial component: influence of metaphyseal shell properties and cement injection depth. Journal of Orthopaedic Research 3: 424-434.
14. Keyak J (2001) Improved prediction of proximal femoral fracture load using nonlinear finite element models. Medical Engineering and Physics 23: 165-173.
15. Cowin SC, Mehrabadi MM (1989) Identification of the elastic symmetry of bone and other materials. Journal of Biomechanics 22: 503-515.
16. Cowin SC, Turner CH (1992) On the relationship between the orthotropic Young's Moduli and Fabric. Journal of Biomechanics 25: 1493-1494.
17. Turner CH, Cowin SC, Rho JY, Ashman RB, Rice JC (1990) The fabric dependence of the orthotropic elastic constants of cancellous bone. Journal of Biomechanics 23: 549-561.
18. Stone JL, Beaupre GS, Hayes WC (1983) Multiaxial strength characteristics of trabecular bone. Journal of Biomechanics 16: 743-752.

19. Bayraktar HH, Morgan EF, Niebur GL, Morris GE, Wong EK, Keaveny TM (2004) Comparison of the elastic and yield properties of human femoral trabecular and cortical bone tissue. Journal of Biomechanics 37: 27-35.
20. Keyak JH, Falkinstein Y (2003) Comparison of in situ and in vitro CT scan-based finite element model predictions of proximal femoral fracture load. Medical Engineering and Physics 25: 781-787.
21. Fenech CM, Keaveny TM (1999) A cellular solid criterion for predicting the axial-shear failure properties of trabecular bone. Journal of Biomechanical Engineering 121: 414-422.
22. Bayraktar HH, Gupta A, Kwon RY, Papadopoulos P, Keaveny TM (2004) The modified super-ellipsoid yield criterion for human trabecular bone. Journal of Biomechanical Engineering 126: 677-684.
23. Niebur GL, Feldstein MJ, Keaveny TM (2002) Biaxial failure behavior of bovine tibial trabecular bone. Journal of Biomechanical Engineering 124: 699-705.
24. Barr AH (1981) Superquadratics and angle-preserving transformations. IEEE Computer Graphics and Applications 1: 11-23.
25. Keaveny TM, Morgan EF, Niebur GL, Yeh OC (2001) Biomechanics of trabecular bone. Annual Review of Biomedical Engineering 3: 307-333.
26. Morgan EF, Bayraktar HH, Keaveny TM (2003) Trabecular bone modulus-density relationships depend on anatomic site. Journal of Biomechanics 36: 897-904.
27. Morgan EF, Yeh OC, Chang WC, Keaveny TM (2001) Nonlinear behavior of trabecular bone at small strains. Journal of Biomechanical Engineering 123: 1-9.
28. Simo JC, Hughes TJR (1998) Computational Inelasticity. Springer-Verlag, New York.
29. Ogden RW (1997) Non-Linear Elastic Deformations. Dover Publications, New York.
30. Borja RI, Sama KM, Sanz PF (2003) On the numerical integration of three-invariant elastoplastic constitutive models. Computer Methods in Applied Mechanics and Engineering 192: 1227-1258.
31. Morman KN (1986) The Generalized Strain Measure with Application to Nonhomogeneous Deformations in Rubber-Like Solids. Journal of Applied Mechanics 53: 726-728.
32. Taylor RL (2003) FEAP - A Finite Element Analysis Program, Users Manual. University of California, Berkeley, CA. Website: http://ce.berkeley.edu/~rlt/feap/.
33. Laib A, Barou O, Vico L, Lafage-Proust MH, Alexandre C, Rugsegger P (2000) 3D micro-computed tomography of trabecular and cortical bone architecture with application to a rat model of immobilisation osteoporosis. Medical and Biological Engineering and Computing 38: 326-332.
34. Fox JC (2003) Biomechanics of the Proximal Femur: Role of Bone Distribution and Architecture. University of California at Berkeley, Berkeley, CA.
35. Yang G, Kabel J, Van Rietbergen B, Odgaard A, Huiskes R, Cowin S (1999) The anisotropic Hooke's law for cancellous bone and wood. Journal of Elasticity 53:125-146.
36. Keyak JH, Rossi SA, Jones KA, Skinner HB (1998) Prediction of femoral fracture load using automated finite element modeling. Journal of Biomechanics 31: 125-133.

1. Initialization:

$$k = 0 \; ; \; \boldsymbol{\varepsilon}^{p^{(0)}} = \boldsymbol{\varepsilon}_n^p \; ; \; \boldsymbol{\alpha}^{(0)} = \boldsymbol{\alpha}_n \; ; \; \beta^{(0)} = \beta_n \; ; \Delta\mu^{(0)} = 0$$

2. Check yield condition and convergence at k^{th} iteration:

$$g^{(k)} = g(\boldsymbol{\varepsilon}^{e^{(k)}}, \boldsymbol{\alpha}^{(k)}, \beta^{(k)}) \; ; \; \left\{\tilde{\mathbf{a}}\right\}^{(k)} = \begin{pmatrix} \mathbf{R}^{(k)} \\ \mathbf{S}^{(k)} \\ T^{(k)} \end{pmatrix}$$

Condition: If $g^{(k)} < tol_1$ and $\left\| \left\{\tilde{\mathbf{a}}\right\}^{(k)} \right\| < tol_2$ then converged.

Else,

3. Compute increment in plasticity parameter:

$$\left[\mathbf{A}^{(k)}\right]^{-1} \; , \; \left\{\tilde{\mathbf{r}}\right\}^{(k)} \; , \; \left\{\partial \mathbf{g}\right\}^{(k)} \text{ and}$$

$$\delta\mu^{(k)} = \frac{-g^{(k)} - \left\{\partial \mathbf{g}\right\}^{(k)} \mathbf{A}^{(k)} \left\{\tilde{\mathbf{a}}\right\}^{(k)}}{\left\{\partial \mathbf{g}\right\}^{(k)} \mathbf{A}^{(k)} \left\{\tilde{\mathbf{r}}\right\}^{(k)}}$$

4. Obtain increment in plastic strain and internal variables:

$$\begin{pmatrix} \Delta\boldsymbol{\varepsilon}^{p^{(k)}} \\ \Delta\boldsymbol{\alpha}^{(k)} \\ \Delta\beta^{(k)} \end{pmatrix} = \mathbf{A}^{(k)} \left\{\tilde{\mathbf{a}}\right\}^{(k)} + \delta\mu^{(k)} \mathbf{A}^{(k)} \left\{\tilde{\mathbf{r}}\right\}^{(k)}$$

5. Update plastic strain and internal variables:

$$\boldsymbol{\varepsilon}^{p^{(k+1)}} = \boldsymbol{\varepsilon}^{p^{(k)}} + \Delta\boldsymbol{\varepsilon}^{p^{(k)}}$$

$$\boldsymbol{\alpha}^{(k+1)} = \boldsymbol{\alpha}^{(k)} + \Delta\boldsymbol{\alpha}^{(k)}$$

$$\beta^{(k+1)} = \beta^{(k)} + \Delta\beta^{(k)}$$

$$\Delta\mu^{(k+1)} = \Delta\mu^{(k)} + \delta\mu^{(k)}$$

$k \leftarrow k+1,$ goto 2.

Box 1 Steps of the implicit return-mapping algorithm.

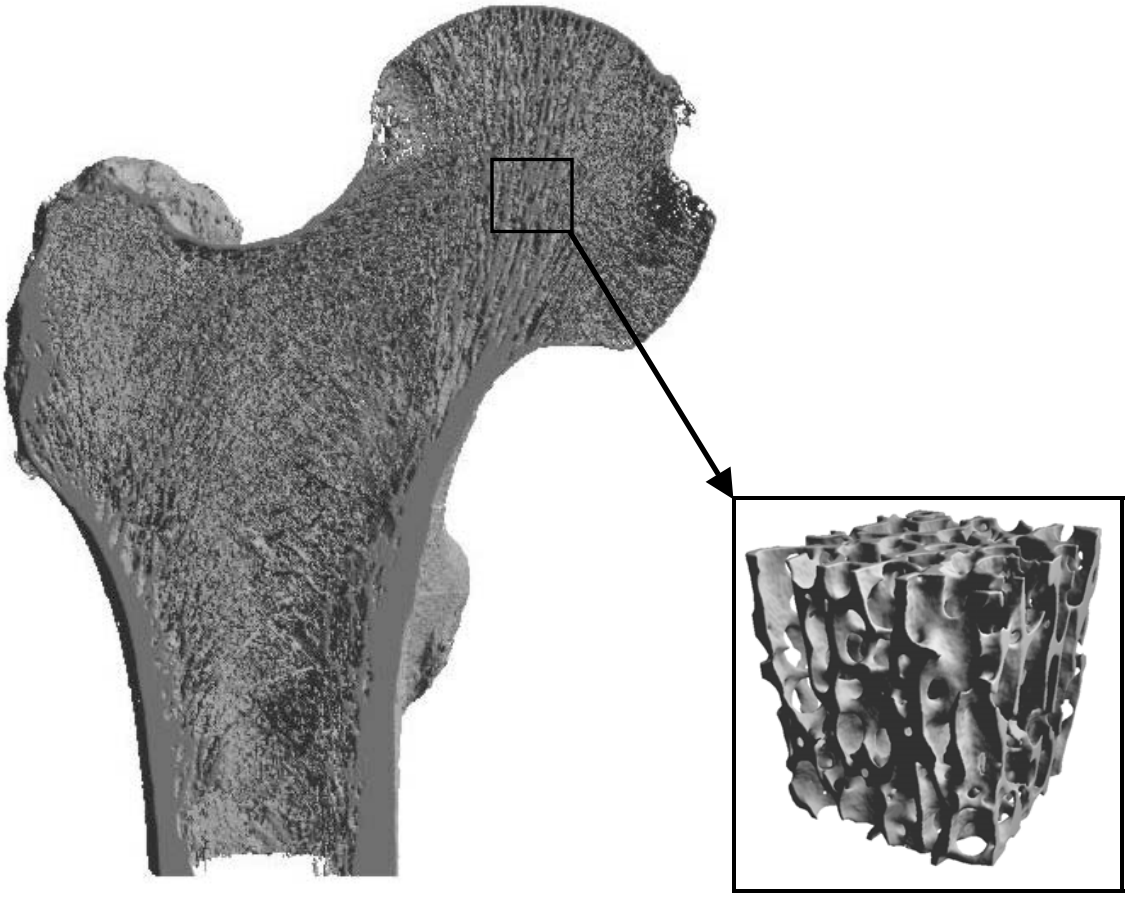

Fig. 1 Three-dimensional rendering of a human proximal femur. The through section cut shows the variation in density and orientation of trabecular bone inside the femur. This image is obtained using micro-Computed Tomography at 89 x 89 x 93 micron resolution (SCANCO, Bassersdorf, Switzerland). The inset shows a representative five-millimeter cubic trabecular bone specimen from the femoral head.

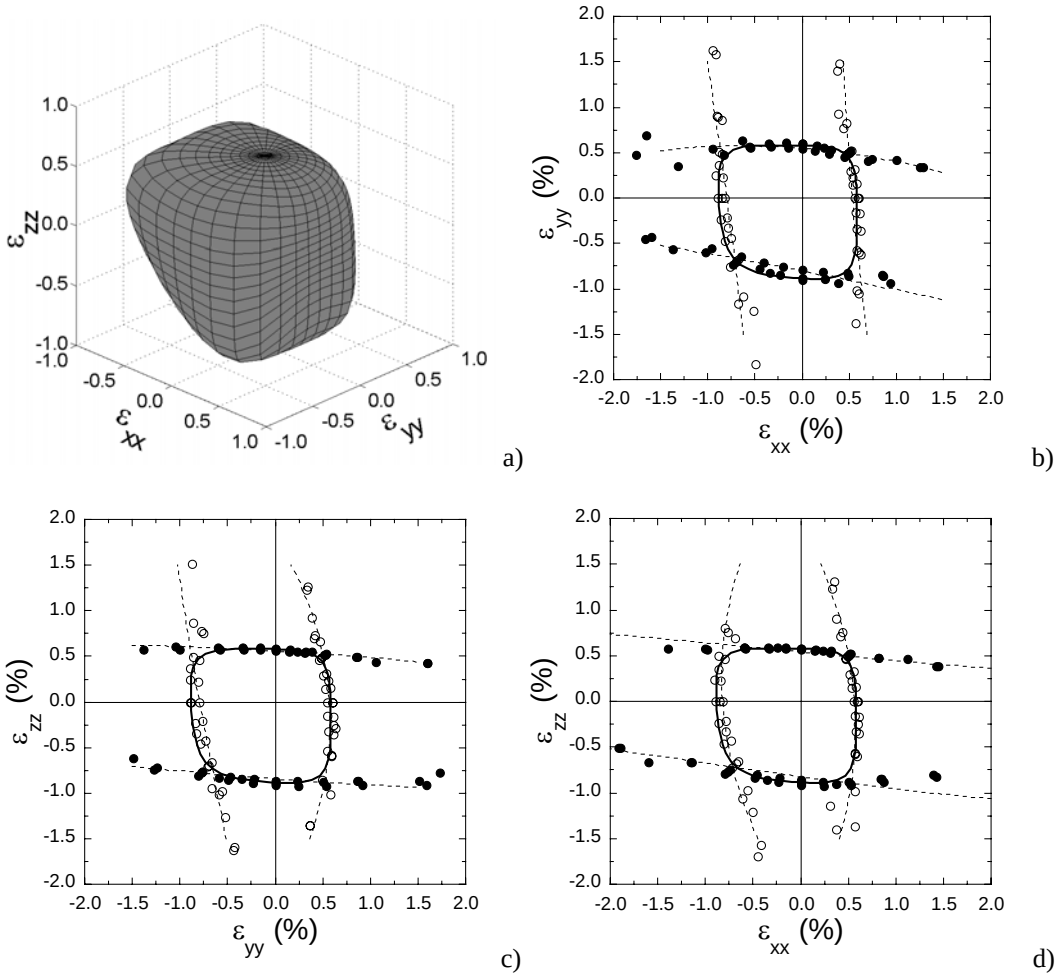

Fig. 2 (a) Complete three-dimensional modified super-ellipsoid yield surface for the femoral trabecular bone based on equation (1) and its cross-section in three mutually perpendicular strain planes: (b) ε_{xx}-ε_{yy}, (c) ε_{yy}-ε_{zz}, and (d) ε_{xx}-ε_{zz}. In (b), (c) and (d) circles indicate the FE computed yield data; solid symbols indicate yielding along the vertical axis; empty symbols indicate yielding along the horizontal axis. Dashed lines shown are quadratic fits to the yield points along each axis (taken from reference [22] with permission).

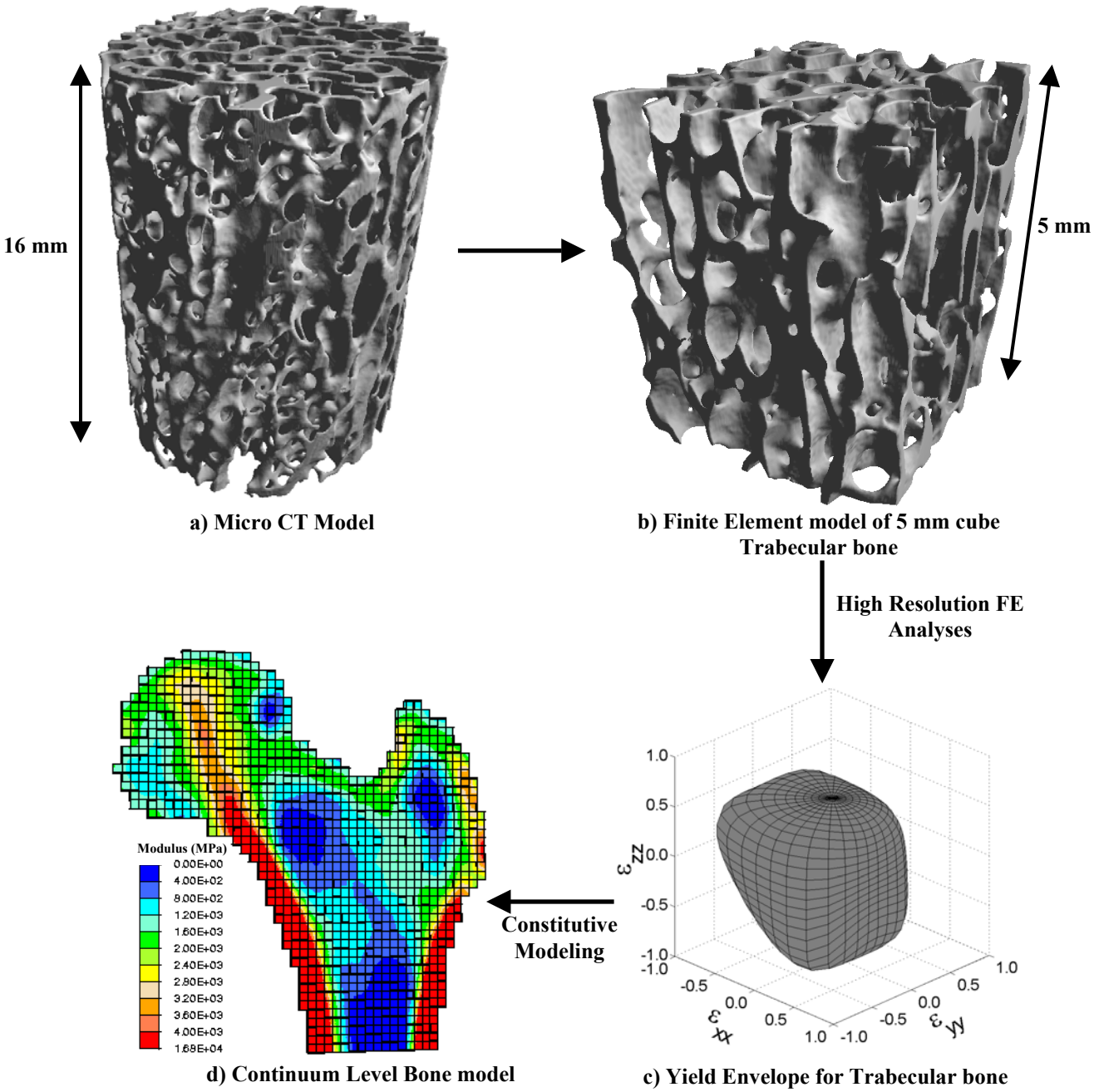

Fig. 3 A flowchart of finite element modeling of proximal femur: a) trabecular bone cylindrical cores (8mm diameter) obtained from proximal femur and scanned using micro-Computed Tomography (μCT) scanner, b) 5 mm cube finite element models generated from these cylinders, c) yield envelope obtained using a series of finite element analyses and optimization using these trabecular bone cube specimens and, d) continuum-level models of whole bone developed and FE analyses performed in which the yield envelope of trabecular bone is included in the material constitutive model. A cross-section of femur with primary elastic modulus distribution is shown here.

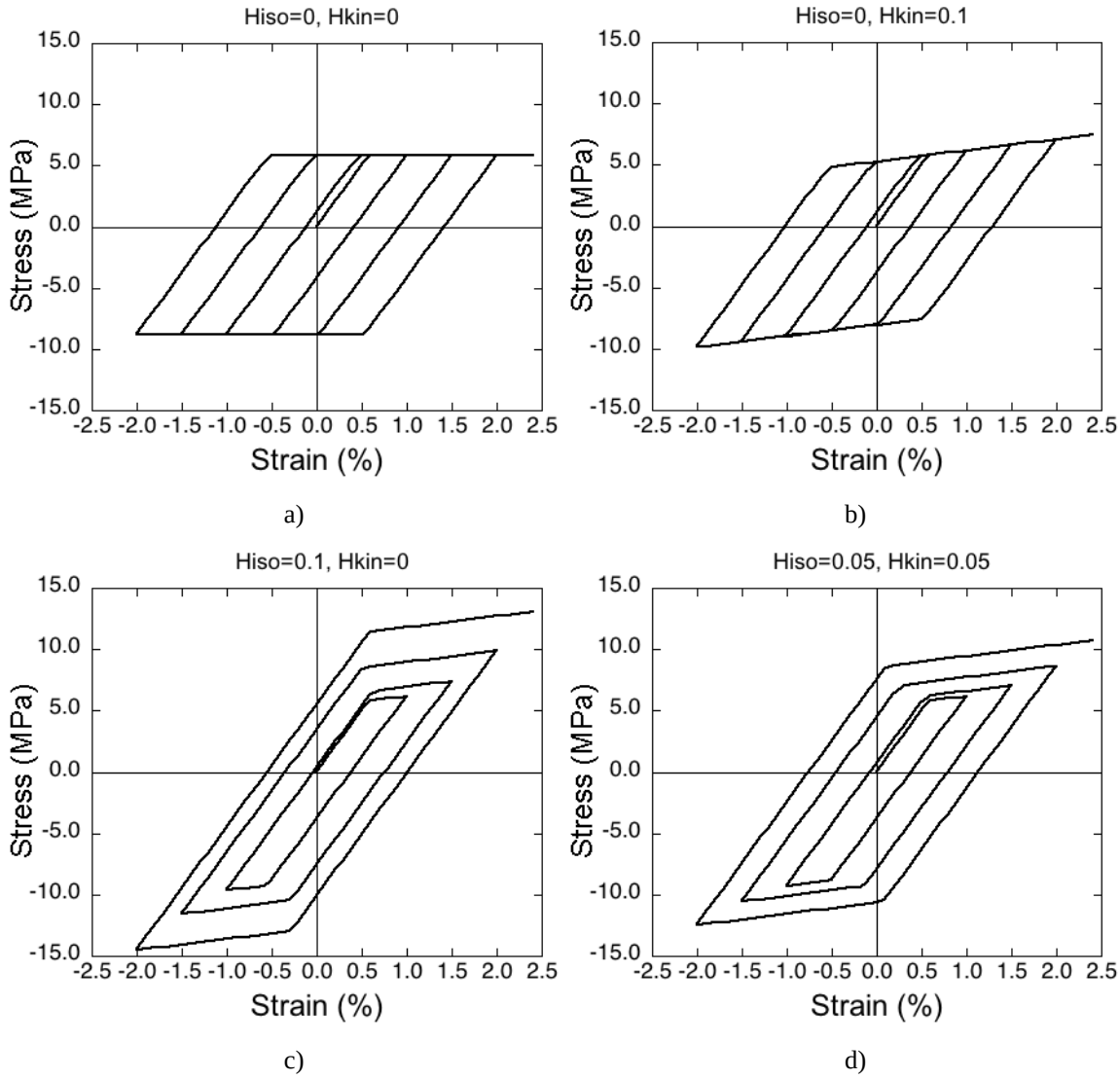

Fig. 4 The stress-strain behavior at one of the integration points of an eight-node brick subjected to cyclic loading. Four test cases are considered assuming material behavior as a) elastic perfectly plastic; b) kinematic hardening 0.1 times the elastic modulus; 3) isotropic hardening 0.1 times the elastic modulus; and 4) both kinematic and isotropic hardening.

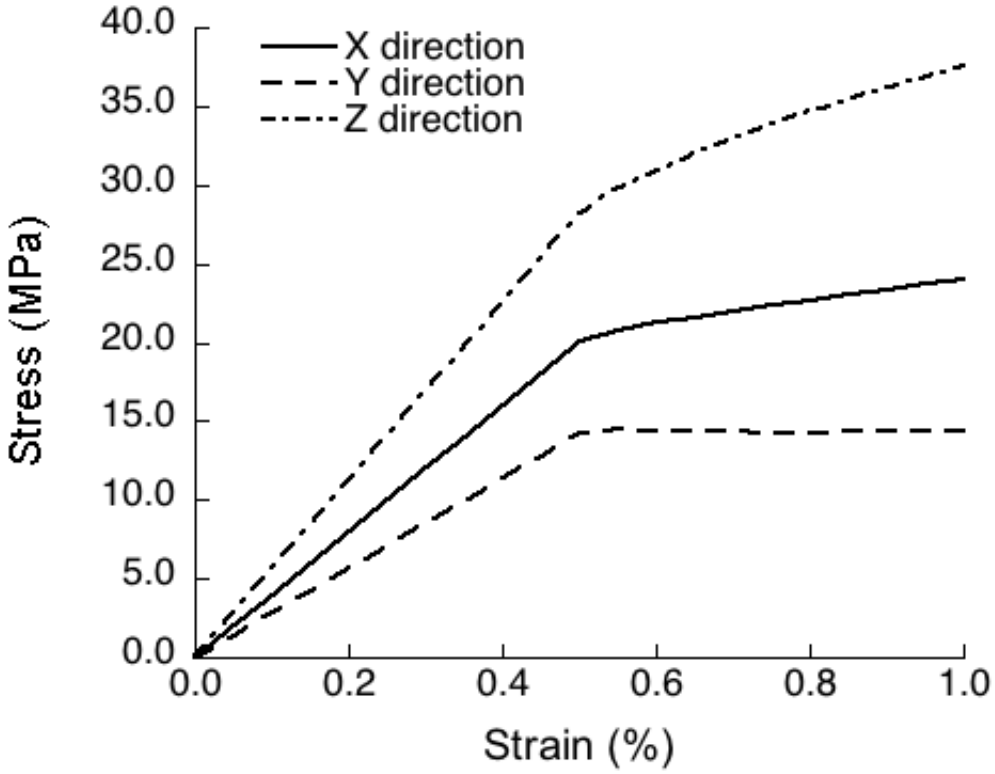

Fig. 5 Stress-strain curves for a 4 x 4 x 4 mm cube model subjected to triaxial compression boundary condition. The model yields at the same strain in three directions but at different stresses.

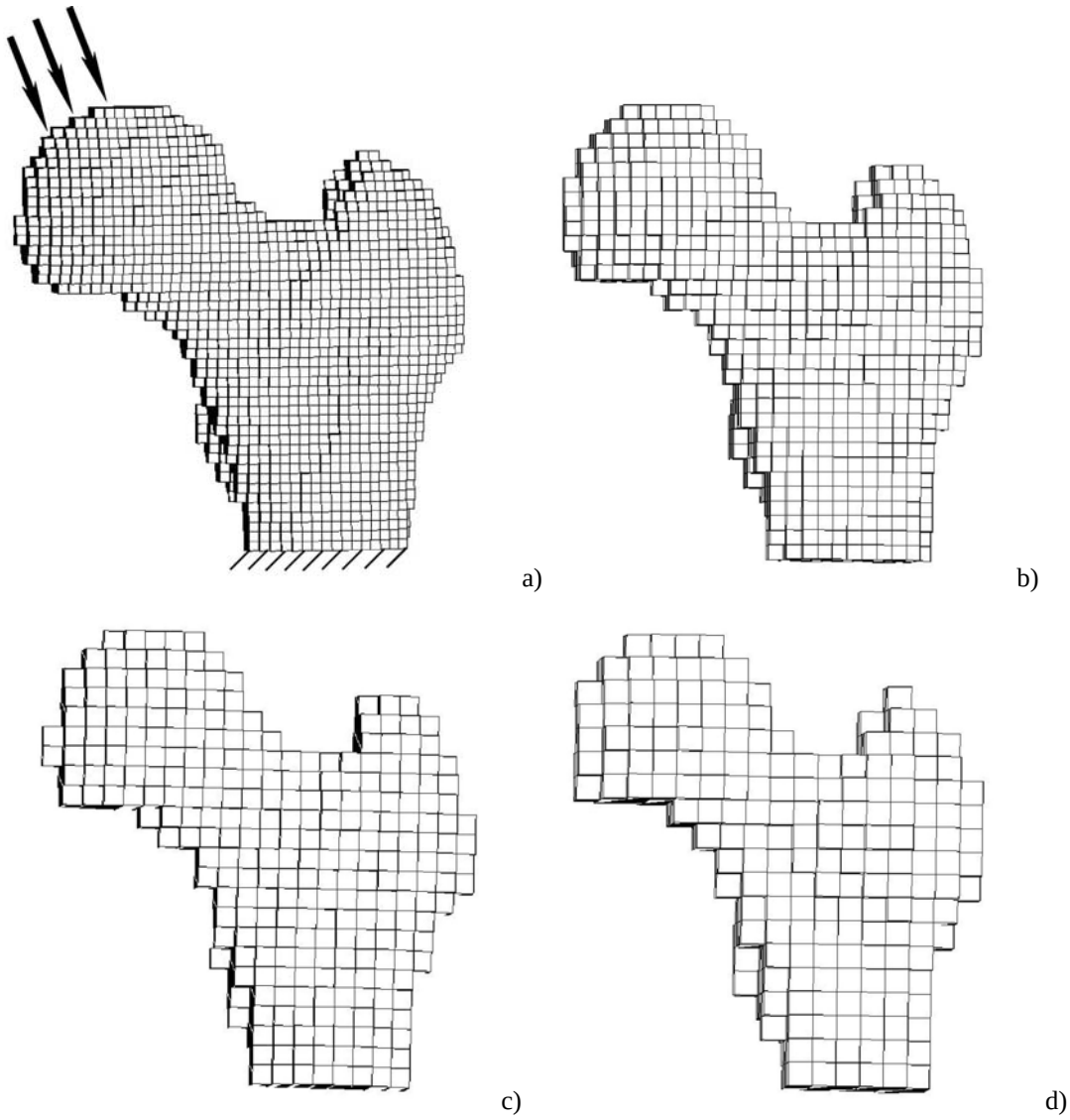

Fig. 6 Finite element models of human femur generated from CT scans of 86 years old female human cadaver with element sizes a) 1.9335 x 1.9335 x 2.0 mm, b) 3.094 x 3.094 x 3.0 mm, c) 4.0604 x 4.0604 x 4.0 mm and, d) 5.0271 x 5.0271 x 5.0 mm having 17516, 4540, 1962, and 1028 elements, respectively. Stance type loading condition, similar to loading of femur in the experiments, is shown for the 2 mm model in which a uniform displacement is applied at femoral head and the distal end is fixed.

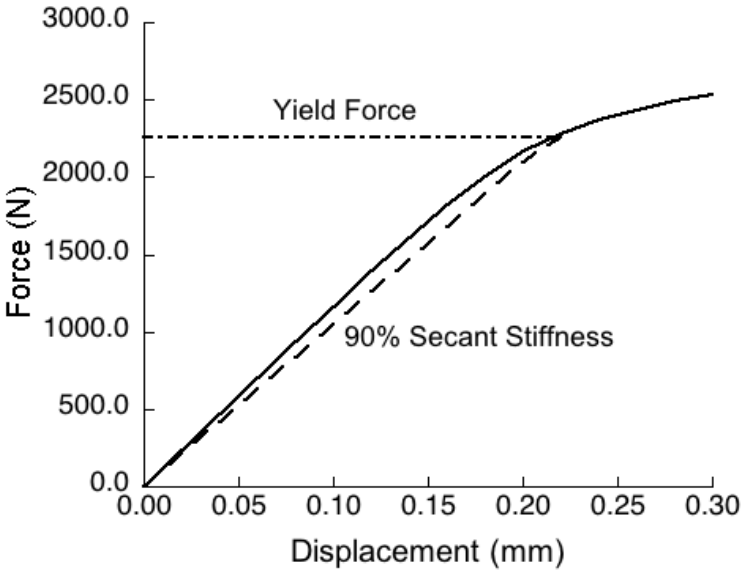

a)

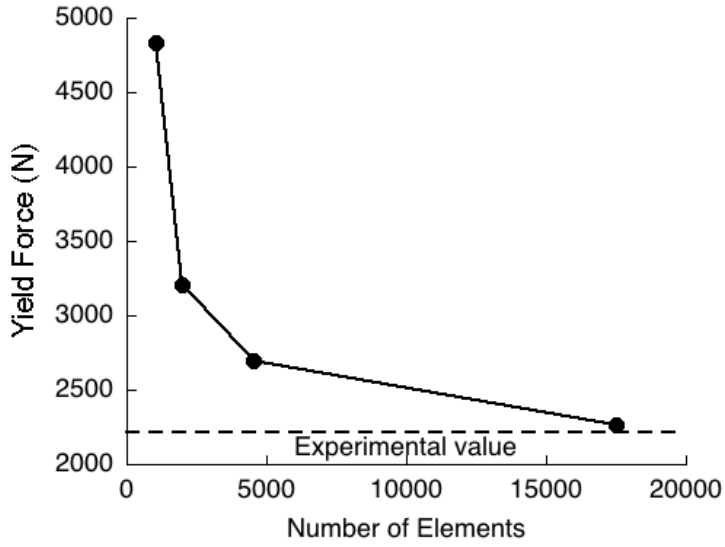

b)

Fig. 7 a) Force-deformation curve for 2mm element size femur model. Yield force is calculated from the force-deformation curve using 90% secant method. b) Convergence behavior of the yield force obtained from FE analysis of femur models where FE results approach actual solution as the mesh resolution is increased from 5mm to 2mm. For comparison experimental yield value is also shown in this figure, which is obtained from destructive testing of this femur.

Table 1 Coefficients of the modified super-ellipsoid yield surface given in equation (1). The radius and center has units of % strain; *n* and *t* are dimensionless.

Coefficient List	
r	0.738
c	-0.157
n	0.414
t	1.417